
Since January 2020 Elsevier has created a COVID-19 resource centre with free information in English and Mandarin on the novel coronavirus COVID-19. The COVID-19 resource centre is hosted on Elsevier Connect, the company's public news and information website.

Biosensors and Bioelectronics 171 (2021) 112753

Contents lists available at ScienceDirect

Biosensors and Bioelectronics

journal homepage: http://www.elsevier.com/locate/bios

# Controlled copper in situ growth-amplified lateral flow sensors for sensitive, reliable, and field-deployable infectious disease diagnostics

Yaofeng Zhou [a,b,1], Yuan Chen [a,d], Yang Liu [c,1], Hao Fang [a,b], Xiaolin Huang [a,b,**], Yuankui Leng [a,b], Zhengqiong Liu [e], Li Hou [d], Wei Zhang [f,***], Weihua Lai [a,b], Yonghua Xiong [a,b,g,*]

[a] State Key Laboratory of Food Science and Technology, Nanchang University, Nanchang, 330047, PR China
[b] School of Food Science and Technology, Nanchang University, Nanchang, 330047, PR China
[c] Department of Clinical Microbiology, The First Affiliated Hospital of Nanchang University, Nanchang, Jiangxi, 330006, PR China
[d] Jiangxi YeLi Medical Device Co. Ltd, Nanchang, 330096, PR China
[e] Department of Clinical Laboratories, Jiangxi Chest Hospital, Nanchang, 330006, PR China
[f] Department of Respiratory Medicine, The First Affiliated Hospital of Nanchang University, Nanchang, Jiangxi, 330006, PR China
[g] Jiangxi-OAI Joint Research Institute, Nanchang University, Nanchang, 330047, PR China

ARTICLE INFO

*Keywords:*
Lateral flow sensor
Gold nanoparticle
Structure-directing agents
Copper in-situ growth
Signal amplification
Infectious disease

ABSTRACT

A polyethyleneimine (PEI)-assisted copper in-situ growth (CISG) strategy was proposed as a controlled signal amplification strategy to enhance the sensitivity of gold nanoparticle-based lateral flow sensors (AuNP-LFS). The controlled signal amplification is achieved by introducing PEI as a structure-directing agent to regulate the thermodynamics of anisotropic Cu nanoshell growth on the AuNP surface, thus controlling shape and size of the resultant AuNP@Cu core–shell nanostructures and confining free reduction and self-nucleation of $Cu^{2+}$ for improved reproducibility and decreased false positives. The PEI-CISG-enhanced AuNP-LFS showed ultrahigh sensitivities with the detection limits of 50 fg $mL^{-1}$ for HIV-1 capsid p24 antigen and 6 CFU $mL^{-1}$ for *Escherichia coli* O157:H7. We further demonstrated its clinical diagnostic efficacy by configuring PEI-CISG into a commercial AuNP-LFS detection kit for SARS-CoV-2 antibody detection. Altogether, this work provides a reliable signal amplification platform to dramatically enhance the sensitivity of AuNP-LFS for rapid and accurate diagnostics of various infectious diseases.

## 1. Introduction

Infectious diseases are usually caused by various pathogens, such as bacteria (Chen et al., 2015), viruses (Brangel et al., 2018), and parasites (Gonçalves et al., 2017). Most infectious diseases are preventable but still associated with considerable morbidity and mortality around the world (Khalil et al., 2018; Reiner et al., 2019). The unknown threats from emerging infectious diseases are particularly increasing with significant effects on the global economy and public health (Grout et al., 2017; Khan et al., 2016). Mitigating global risk of infectious diseases requires versatile, rapid, and portable sensing tools of pathogens (Wood et al., 2019). Although the nucleic acid test by using molecular diagnostic systems, such as reverse transcription polymerase chain reaction (RT-PCR), is well-accepted as the current standard method for diagnosing pathogen infection (Cao-Lormeau et al., 2016; Santiago et al., 2018), it usually suffers from limitations, including complex operation, long turnaround time, and the requirement of costly reagents, specialized instruments, certified laboratories, and skilled technicians (Xiao et al., 2018). In addition, high false negative rates are another concern (López-Ríos et al., 2004). These limitations compromise the accessibility of such tests for rapid and accurate identification of infectious diseases at the point of care (POC) (Kim et al., 2017a).

The sensitive detection of special biomarkers against pathogens, such as antigens, antibodies (Abs), or pathogens themselves, is an alternative

* Corresponding author. State Key Laboratory of Food Science and Technology, Nanchang University, Nanchang, 330047, PR China.:
** Corresponding author. School of Food Science and Technology, Nanchang University, Nanchang, 330047, PR China.,
*** Corresponding author.
*E-mail addresses:* hxl19880503@163.com, xiaolin.huang@ncu.edu.cn (X. Huang), zhangweiliuxin@163.com (W. Zhang), yhxiongchen@163.com (Y. Xiong).
[1] These authors contributed equally to this work.

https://doi.org/10.1016/j.bios.2020.112753
Received 14 June 2020; Received in revised form 13 October 2020; Accepted 20 October 2020
Available online 21 October 2020

to assist the rapid diagnosis of infection (Kurdekar et al., 2018; Zhang et al., 2017). Gold nanoparticle-based lateral flow sensor (AuNP-LFS) is one of the most prominent POC diagnostic tools in the field detection (Zhou et al., 2019). The fine accuracy and operability of AuNP-LFS have promoted thorough investigations of stringent issues, including serological testing of pathogens (Chen et al., 2020; Gao et al., 2017). However, the concentrations of serum biomarkers against pathogens at the early stage of infection, recovery, and after-drug treatment are far below the detection limit (LOD) of conventional field-deployable AuNP-LFS, which are limited by the low capture efficiency (<5%) of AuNP probes at the test (T) zone and the weak colorimetric signal brightness of AuNPs (Jiang et al., 2018; Zhan et al., 2017). Consequently, false negatives for conventional AuNP-LFS are often observed, thereby resulting in misdiagnosis of positive patients, increasing the risk of the disease spread, and constraining the outbreak containment endeavor (You et al., 2017).

Signal amplification technologies, such as metal in-situ growth (MISG) (Huang et al., 2018a; Kim et al., 2017b), NP accumulation (Tang et al., 2009), and enzyme catalytic deposition (Loynachan et al., 2018), are attracting considerable attention due to their strong signal amplification capability to improve the sensitivity of traditional AuNP-LFS. MISG strategies exhibit potential in practical applications due to their superior signal amplification and simple operation. Gold- and silver-based MISG strategies are the most commonly used strategies for amplifying the optical signal of AuNPs (Huang et al., 2016). Compared with gold or silver growth, copper growth shows more outstanding potential in enhancing the sensitivity of AuNP-LFS. Li et al. reported a copper deposition-assisted method to amplify the AuNP-LFS for the sensitive detection of human chorionic gonadotropin with the LOD of 1 pg $mL^{-1}$, with *ca.* two to three orders of magnitude improvement than that of conventional AuNP-LFS (Tian et al., 2019). Nonetheless, in traditional MISG, the metal ions (i.e., Au, Ag, and Cu) are directly bound with protein or capping agents on the surface of AuNP probes and reduced to metal shell in the presence of reducing agents. However, this layer-by-layer growth pattern by direct deposition of metal shell on the AuNP surface shows several limitations: 1) metal ions can produce strong nonspecific binding on proteins and nitrocellulose (NC) membrane, 2) metal ions can undergo self-nucleation independent of AuNP probes under excessive reducing agents, and 3) the layer-by-layer growth pattern is uncontrollable on the NC membrane. These issues would cause strong background on NC membrane, low reproducibility, and false positives, severely restricting the practical applications of MISG.

Structure-directing agents (SDAs) play a key role in controlling the shape and size of NPs (Sun and Xia 2002b; Wang et al., 2017). In general, SDAs show dual functions during the controlled synthesis of NPs (Washio et al., 2006): (i) SDAs limit the crystal growth and control the NP size through their strong interaction with the metal plane indexed as (100) (Skrabalak et al., 2007), and (ii) SDAs can serve as a stabilizer to prevent the free reduction and self-nucleation of metal ions through the strong chelate interaction between SDAs and metal ions (Da Silva et al., 2016). Numerous polymer-type SDAs, such as poly(vinyl alcohol) (Xiong et al., 2006), polyacrylic acid(Lu et al., 2001), polyethyleneimine (PEI) (Li et al., 2013), and poly(vinyl pyrrolidone) (Sun and Xia 2002a), have been extensively explored to control the seed-mediated crystal growth for the synthesis of core–shell nanostructures with a well-defined shape and size. These polymers are generally anchored on the surface of seed NPs, and the metal ions are then bound with the polymer skeleton through the strong metal coordination interaction. Given that the polymer content absorbed on the seed surface is directly proportional to the seed amount, the size of grown core–shell nanostructures is theoretically controllable (Xia et al., 2017). Besides, the preferential binding of polymers to metal plane (100) allows the regulation of the shape and thermodynamics of anisotropic growth of the resultant nanostructures (Chen et al., 2019). Therefore, SDA-assisted control of MISG on the surface of AuNP probes at the T line possibly contributes to improving the robustness, stability, and reproducibility of conventional MISG-based signal amplification.

In this work, we report the use of a polymer-type SDA (PEI) to assist in copper in-situ growth (PEI-CISG) on the surface of AuNP probes for significantly amplifying the detection signal of traditional AuNP-LFS. In this design, $Cu^{2+}$ solution was pre-incubated with PEI to form the PEI@$Cu^{2+}$ complex *via* the strong chelation of $Cu^{2+}$ with the amino groups of PEI. The as-prepared PEI@$Cu^{2+}$ complex was adsorbed on the surface of AuNP probes. Then, PEI was used as the template skeleton to control the copper reduction and growth in the presence of mild reducing agent, that is, sodium ascorbate (VcNa; Scheme 1). With the copper shell growth and deposition on the surface of AuNP probes assembled on the T and control (C) lines *via* antigen–Ab interactions, the colorimetric signal intensities of AuNPs were significantly enhanced, which can transform the T line on the NC membrane from completely white (invisible) to a red band (visible). The originally undetectable AuNP binding at the T area induced by low concentration of the target can be considerably amplified and detected by this strategy. In addition, the chelation of $Cu^{2+}$ with PEI to form the PEI@$Cu^{2+}$ complex can efficiently suppress the free reduction and self-nucleation of $Cu^{2+}$ in the presence of VcNa without the aid of AuNP co-reduction, thereby preventing the occurrence of false positives. We further investigated the potential of our designed PEI-CISG-assisted signal amplification combined with the sandwich AuNP-LFS as an alternative rapid diagnostic platform for quickly responding to three infectious diseases caused by bacteria and viruses. Human immunodeficiency virus (HIV) type 1 capsid p24 antigens against HIV infection, which causes acquired immunodeficiency syndrome, and severe acute respiratory syndrome coronavirus 2 (SARS-CoV-2) Abs against SARS-CoV-2 virus infection, which causes the novel coronavirus disease (COVID-19), were selected as typical serological model biomarkers of antigens and Abs, respectively, whereas *Escherichia coli* O157:H7 (*E. coli* O157:H7), which is a common foodborne pathogen with strong pathogenicity at about 10 CFU of live bacteria, was selected as a model pathogen. Under the developed conditions, we successfully achieved the ultrasensitive detection of p24 antigen in serum and *E. coli* O157:H7 in milk with LODs of 50 fg $mL^{-1}$ and 6 CFU $mL^{-1}$, respectively. We completed the clinical studies to validate the clinical diagnostic efficacy of this improved approach by integrating a commercial AuNP-LFS detection kit for SARS-CoV-2 Abs. Results showcased that this commercial strip can efficiently eliminate false negative detection and largely improve clinical COVID-19 diagnosis after equipping with our proposed PEI-CISG. In short, the designed PEI-CISG technology presents the huge potential as a versatile signal amplification platform for improved AuNP-LFS with acceptable accuracy and reproducibility, contributing to the clinical diagnostic testing of pathogen infections.

## 2. Experiment section

### 2.1. Materials

Chloroauric acid ($HAuCl_4$), copper chloride ($CuCl_2$), PEI, VcNa, trisodium citrate, biotin-3-sulfo-N-hydroxysuccinimide ester sodium salt, SA, procalcitonin (PCT), human serum albumin (HSA), prostate-specific antigen (PSA), C-reactive protein (CRP), alpha-fetoprotein (AFP), were purchased from Sigma-Aldrich Chemical Co (St. Louis, MO). The sample pad, NC membrane, and an absorbent pad were obtained from Schleicher and Schuell GmbH (Dassel, Germany). Anti-p24 cAbs (5.0 mg $mL^{-1}$) and dAbs (6.4 mg $mL^{-1}$) were provided by Abcam (Cambridge, MA). Anti-*E. coli* O157:H7 dAbs (2 mg $mL^{-1}$) and cAbs (2 mg $mL^{-1}$), goat anti-mouse IgG (10 mg $mL^{-1}$), and BSA were purchased from Meridian Life Science, Inc (Memphis, TN, USA). The commercial AuNP-LFS detection kit for SARS-CoV-2 Abs was provided by Jiangxi YeLi Medical Device Co., Ltd (Nanchang, China).

*E. coli* O157:H7 (ATCC43888), *Salmonella choleraesuis* (ATCC 10708), *Salmonella anatis* (ATCC 9270), *Salmonella enteritidis* (ATCC 13076), *Salmonella typhimurium* (ATCC 13311), *Salmonella paratyphi* A

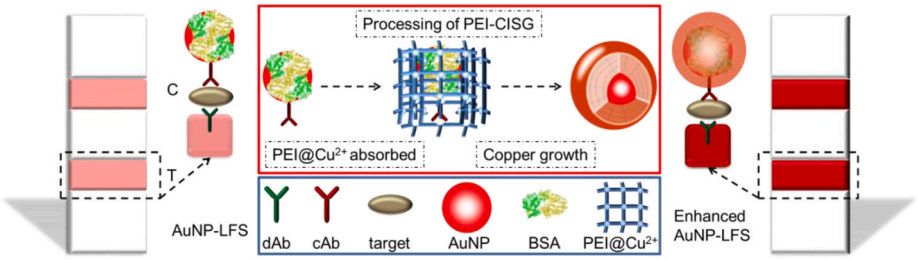


**Scheme 1.** Schematic illustration of the principle and process of PEI-CISG technology for enhancing AuNP-LFS.

(ATCC 9150), *Listeria grayi* (ATCC 25410), *L. iuanuii* (ATCC 1911), and *L. seeligeri* (ATCC 35967) were obtained from the American Type Culture Collection. *L. monocytogenes* (CMCC 54001), *L. monocytogenes* (CMCC 54007), *Enterobacter sakazakii* (CMCC 45401), *Enterobacter sakazakii* (CMCC 45402), *Staphylococcus aureus* (CMCC 26001), *Staphylococcus aureus* (CMCC 26002), *Micrococcus luteus* (CMCC 28001), *Proteusbacillus vulgaris* (CMCC 49027), and *Serratia marcescens* (CMCC 41002) were obtained from The Inquiry Network for Microbial Strains of China.

### 2.2. Instrument and characterization

The shape and size of AuNPs before/after PEI-CISG treatment were characterized using a JEM-2100 SEM (JEOL, Japan) and TEM (JEOL, Japan). UV–visible absorption spectra were recorded on a UV–vis spectrophotometer (Thermo Fisher, G10S, USA). DLS measurement was conducted on a Malvern Nano-Z90 zetasizer (Malvern Instruments, Worcestershire, UK). A commercial HG-8 portable strip reader was obtained from Shanghai Huguo Science Instrument Co., Ltd (Shanghai, China). A BioDot XYZ platform combined with a motion controller, a BioJet Quanti3000k dispenser, and an AirJet Quanti3000k dispenser for solution dispensing were supplied by BioDot (Irvine, CA). An automatic programmable cutter was purchased from Jinbiao Biotechnology Co., Ltd (Shanghai, China).

### 2.3. Bacteria and culture conditions

*E. coli* strains were cultured in Luria–Bertani medium at 37 °C for 12 h. *L. monocytogenes* was cultured in brain heart infusion broth for 18 h at 37 °C, and *Vibrio parahaemolyticus* was inoculated in Luria–Bertani medium with 3% NaCl at 37 °C for 18 h. Other strains were grown in Luria–Bertani medium at 37 °C for 18 h. *E. coli* O157:H7 culture was harvested by undergoing centrifugation at 5000 rpm for 20 min at room temperature. The bacterial cells were then washed thrice and resuspended in sterile phosphate-buffered saline (PBS).

### 2.4. Synthesis of AuNPs

AuNPs of size 37 ± 6 nm were synthesized on the basis of a previous method (Huang et al., 2018b). Briefly, 100 mL $HAuCl_4$ solution (0.1% w/v) was heated until boiling, and 1.5 mL 1% (w/v) trisodium citrate solution was rapidly added under constant stirring. The mixture solution was kept boiling for another 10 min. The synthesized AuNP solution was cooled down to room temperature for further use.

### 2.5. Preparation of AuNP@dAb

The AuNP@dAb probes against anti-p24 or *E. coli* O157:H7 were prepared in accordance with a previous report (Huang et al., 2019). In a typical procedure, 1 mL citrate-coated AuNP solution was first adjusted to the appropriate pH with 0.01 M $K_2CO_3$. Under gentle stirring, 4 μL anti-p24 or anti-*E. coli* O157:H7 dAb solution was dropwise added to the AuNP solution, and the resulting mixture was incubated for 1 h under stirring at room temperature. The reacted AuNPs were further blocked by adding 6 μL blocking solution containing 10 mg $mL^{-1}$ BSA for another 1 h. The reaction mixture was centrifuged under 10,000 rpm at 4 °C for 10 min to remove the unreacted reagents, and the precipitates were resuspended in 0.01 mM PBS solution containing 5% sucrose, 2% trehalose, 1% PEG 20,000, 1% BSA, and 0.25% Tween-20 with pH 7.2.

### 2.6. Fabrication of LFS

The cAbs against p24 or *E. coli* O157:H7 (1 mg $mL^{-1}$) and goat anti-mouse IgG (2 mg $mL^{-1}$) were spotted on the NC membrane as the T and C lines, respectively. The conjugate pads were prepared by spraying 30 pM AuNP@dAb for p24/AuNP@dAb for *E. coli* O157:H7 and drying at 37 °C overnight. The strip assembly was conducted following our previous work (Hao et al., 2020).

### 2.7. Detection procedure of our LFS

About 75 μL sample solution was directly added into the sample well of the strip. After a 10 min reaction, the optical densities (ODs) of T and C lines on the NC membrane were collected by using the HG-8 strip reader.

### 2.8. PEI-CISG amplification procedure

The reacted strip was first immersed in the PEI@$Cu^{2+}$ complex solution, which was prepared by adding 5 mL $Cu^{2+}$ solution to 5 mL PEI solution under gentle stirring. After 5 min, the as-prepared strip was moved to ultrapure water solution (18.2 M) to remove the nonspecifically adsorbed PEI@$Cu^{2+}$. Finally, the strip was transferred to 100 mg $mL^{-1}$ VcNa solution for 2 min. The ODs at the T and C lines were collected by using the HG-8 strip reader.

## 3. Results and discussion

### 3.1. Controlled PEI-CISG signal amplification on NC membrane

Bovine serum albumin (BSA)-coated AuNPs (AuNP@BSA) were first used as an alternative of AuNP@Abs to confirm the feasibility of PEI-CISG-based controlled signal amplification on NC membrane. AuNPs (37 ± 6 nm, $n$ = 100) were synthesized by using a classical citrate reduction method (Zhou et al., 2018) and then conjugated with BSA to prepare the AuNP@BSA *via* electrostatic adsorption (Liu et al., 2013). The obtained AuNP@BSA exhibited an evident red shift of surface plasmon resonance absorption peak with an increased hydrodynamic diameter ($D_H$), indicating the successful coating of BSA protein on the AuNP surface (Fig. S1). Subsequently, the AuNP@BSA (1 mg $mL^{-1}$) was sprayed onto the NC membrane as T line, and BSA solution (1 mg $mL^{-1}$) was used as the control group. The PEI-CISG-based signal amplification was performed by immersing the two strips in a premixed PEI@$Cu^{2+}$ solution for 5 min. The successful absorption of PEI@$Cu^{2+}$ complex onto the surface of AuNP@BSA probe was confirmed with these characterizations, including UV–Vis absorption spectra, infrared spectra and Raman spectra (Fig. S2). Thereafter, the soaked strip was transferred

into ultrapure water for 1 min to remove the nonspecifically adsorbed PEI@$Cu^{2+}$ and then immersed in the reduction solution containing 100 mg $mL^{-1}$ VcNa for 2 min. The ODs of the enhanced strip were recorded by using a strip reader. Fig. 1a shows that the PEI-CISG-enhanced strip sprayed with AuNP@BSA had a remarkably increased OD value when compared to the strip without treatment. The corresponding stereograms of the strips are shown in the inset of Fig. 1a. Scanning electron microscopy (SEM) images of the enhanced strip showed a mass of significantly enlarged particles distributed in the NC membrane pores, suggesting the formation of AuNP@Cu core–shell nanostructure (Fig. 1b and c). Energy-dispersive X-ray (EDX) spectroscopy shown in Fig. 1d indicates the presence of Cu element, showing the successful growth and deposition of Cu shell on AuNP surface. Transmission electron microscopy (TEM) images indicate that the enlarged nanocomposite exhibited a characteristic core–shell nanostructure with the Cu nanoshell around the Au core (Fig. 1e and f), which was further verified by high-angle annular dark-field scanning TEM elemental mapping (Fig. 1g). Powder X-ray diffraction pattern (Fig. S3a) and X-ray photoelectron spectrum (Fig. S3b) prove the coexistence of Au and Cu element in the formed AuNP@Cu nanocomposite. Additionally, the strip sprayed with only the BSA solution showed no enhanced band at the T line after PEI-CISG treatment. The above results demonstrate that the $Cu^{2+}$ chelated by using PEI cannot be reduced to Cu nanocrystal by using VcNa, thereby effectively circumventing false positives that originate from the self-nucleation of $Cu^{2+}$. However, with the aid of AuNP synergistic promoter, the PEI@$Cu^{2+}$ is prone to be reduced to Cu nanoshell by using VcNa to form AuNP@Cu core–shell nanocomposites at the T line, dramatically promoting the signal amplification of the strip. The reproducibility of the amplified strip is another important issue for its practicality. Thus, a series of strips sprayed with different concentrations of AuNP@BSA from 0 pM to 10 pM was used in the PEI-CISG experiment with six replicates. Fig. S4a presents a prototype set of test strips at each concentration after PEI-CISG treatment. The color on T line gradually deepened with the increase in AuNP@BSA concentration, whereas no red bands at the T line were observed when the enhanced strips were used in the absence of AuNP@BSA. The corresponding OD values at each AuNP@BSA concentration were then summarized (Figs. S4b–S4e, Table S1, and Fig. 1h). The results in Fig. 1h and Table S1 show that the variable coefficient of OD values of the enhanced strips at each AuNP@BSA concentration ranged from 1.73% to 2.96%, revealing the acceptable reproducibility of our PEI-CISG signal amplification. Notably, the OD values of the enhanced strips showed a good linearity against the concentration of AuNP@BSA on T line with $R^2$ of 0.9922 (Fig. 1h), implying that the PEI-CISG-amplified strip is suitable for the accurate quantitative detection of targets.

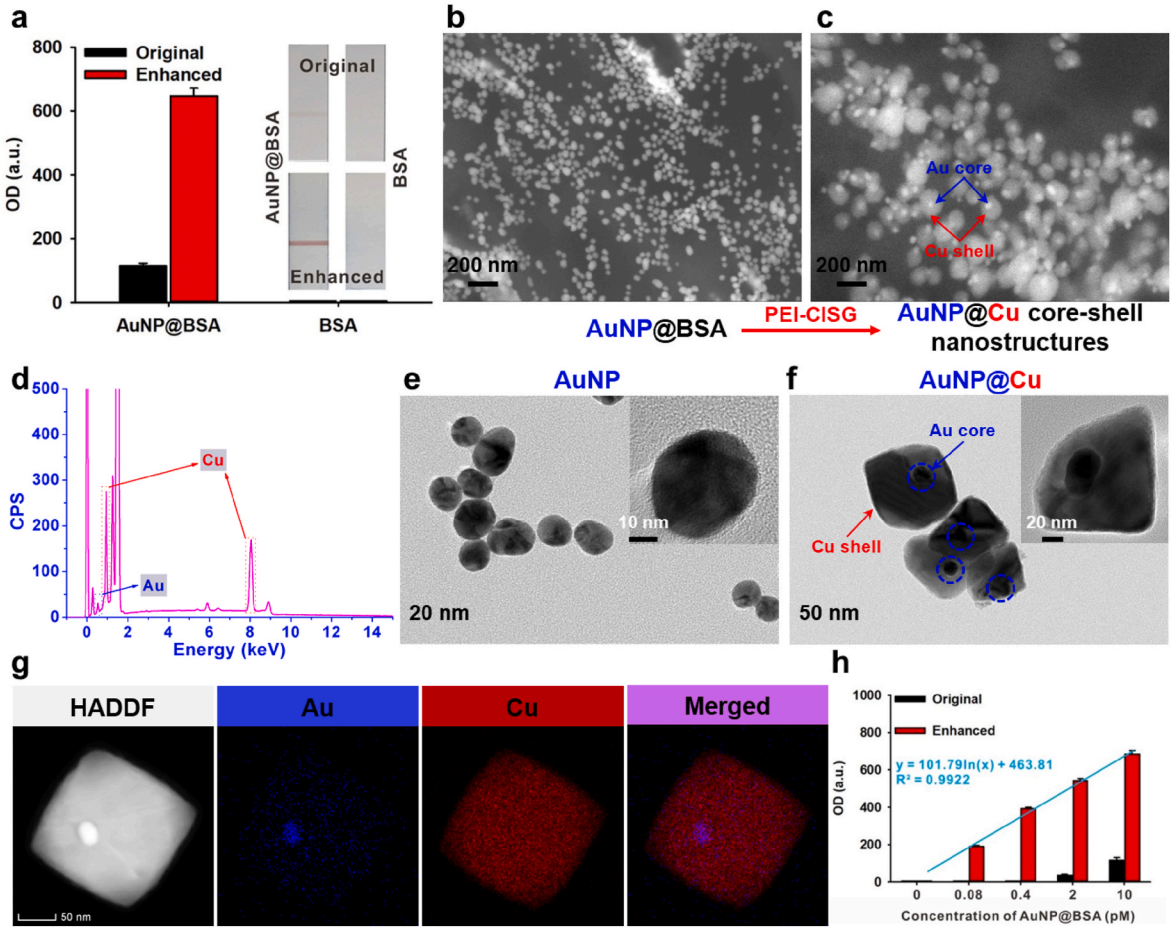


**Fig. 1.** Feasibility analysis of PEI-CISG technology conducted on AuNP-LFS. (a) Confirmation of PEI-CISG strategy for enhancing AuNP@BSA and BSA spayed strip. After PEI-CISG treatment, the markedly enhanced signal intensity was only observed in AuNP@BSA spayed strip, while negligible changes occurred in BSA spayed strip, including that the Cu shell growth is dependent of Au core. The inset is the strip prototypes before and after PEI-CISG treatment. SEM images for validating the Cu shell growth on AuNP surface on the NC membrane before (b) or after (c) PEI-CISG. (d) Energy dispersive X-ray spectrometry (EDS) analysis of AuNPs after PEI-CISG. TEM images for verifying the Cu shell growth on AuNP surface in solution before (e) or after (f) PEI-CISG. The inset of Fig. 1e and f indicate high magnification of individual AuNP and AuNP@Cu. Results demonstrate the formation of AuNP@Cu core-shell nanostructure after PEI-CISG treatment. (g) HAADF-scanning TEM EDS elemental mapping analysis of AuNP@Cu. (h) The correlative curve of OD value against AuNP@BSA concentration obtained with or without PEI-CISG enhancement.

### 3.2. Optimization of PEI-CISG on NC membrane

The concentrations and ratio of PEI and $Cu^{2+}$ were the most important parameters that influenced the controlled growth and synthetic yield of Cu nanostructures. First, the ratio of PEI and $Cu^{2+}$ in the PEI@$Cu^{2+}$ solution was optimized, in which the PEI concentration was 1 mg $mL^{-1}$, and those of $Cu^{2+}$ were 0.5, 1, 2, 3, and 4 mg $mL^{-1}$. The difference in ODs (Δd) on the T line before and after PEI-CISG treatment was used to confirm the optimum parameter. The results in Fig. 2a show that Δd increased sharply as $Cu^{2+}$ concentration was raised from 0.5 mg $mL^{-1}$ to 2 mg $mL^{-1}$, indicating that increased $Cu^{2+}$ concentration can effectively improve the synthetic yield of Cu nanoshell. However, the further increase in $Cu^{2+}$ concentration (3 and 4 mg $mL^{-1}$) conversely caused a decrease in Δd. This phenomenon possibly occurred because excessive amounts of $Cu^{2+}$ could occupy most of the amino functional groups of PEI molecule and reduce the binding of PEI@$Cu^{2+}$ complex to AuNP@BSA, thereby resulting in a poor Cu nanoshell in-situ growth. Subsequently, the concentration of PEI@$Cu^{2+}$ complex was further optimized by changing the PEI content from 1 mg $mL^{-1}$ to 10 mg $mL^{-1}$ at the optimal PEI and $Cu^{2+}$ ratio of 1:2 (m/m). Fig. 2b shows that Δd gradually increased as the amounts of PEI@$Cu^{2+}$ complex increased, indicating that high concentration PEI@$Cu^{2+}$ solution contributed to the adsorption of AuNP@BSA to the PEI@$Cu^{2+}$ complex. However, Δd conversely decreased when the PEI concentration further increased to 7.5 mg $mL^{-1}$. We speculate that the high viscosity of PEI@$Cu^{2+}$ complex with high PEI concentration (>7.5 mg $mL^{-1}$) could hamper the PEI@$Cu^{2+}$ penetrability into the pores of NC membrane, thereby leading to a low adsorption of AuNP@BSA to the PEI@$Cu^{2+}$ complex. Thus, the optimum PEI@$Cu^{2+}$ solution was suggested to contain 5 mg $mL^{-1}$ PEI and 10 mg $mL^{-1}$ $Cu^{2+}$. Furthermore, the soaking time of the strip in PEI@$Cu^{2+}$ solution and the subsequent copper growth time in VcNa solution were carefully optimized. Fig. 2c shows that the highest Δd was achieved with the strip soaking time of 5 min and copper growth time of 2 min, indicating that the PEI-CISG executed on the strip platform can be fully completed within 8 min. These findings suggest that the PEI-CISG method is an ideal signal amplification strategy to meet the rapid detection requirement for POC diagnostics.

In a conventional sandwich AuNP-LFS system, the capture efficiency of AuNP probes at the T line is usually less than 5% and shows a huge difference due to the varied binding affinity among different antigen–Ab pairs (Duan et al., 2017). The high affinity binding system of biotin–streptavidin (SA; $K_D = 10^{-15}$ M) (Aissa et al., 2017) was applied to simulate the capture of AuNP probes at the T line and further evaluate the potential of our PEI-CISG signal amplification strategy to improve the sensitivity of sandwich AuNP-LFS (Fig. 2d). UV–visible absorption spectra and dynamic light scattering (DLS) measurement (Fig. S5) demonstrated the successful conjugation of AuNPs with SA (AuNP@SA). Subsequently, 75 μL AuNP@SA probe solution with the concentrations ranging from 300 pM to 0.03 fM was used to run the strip, in which BSA@biotin (1 mg $mL^{-1}$) was sprayed on the NC membrane as a T line. The reacted strips were then treated by using the PEI-CISG signal amplification system and the results with and without PEI-CISG treatment are displayed in Fig. 2e. When the unamplified AuNP-LFS strip was used, the linear correlation between the OD values and the logarithmic concentration of AuNP@SA ranged from 3 pM to 300 pM, with LOD of 3 pM. By contrast, after the PEI-CISG amplification, the enhanced AuNP-LFS provided a wider linear detection range from 0.3 fM to 300 pM, with LOD of 0.3 fM, which was about four orders of magnitude lower than that of the AuNP-LFS without PEI-CISG treatment. In addition, we found that the amplification capacity of the designed PEI-CISG technology was not affected by humidity and temperature (Fig. S6). These results indicate that the PEI-CISG strategy exhibits huge potential to improve the detection sensitivity of conventional AuNP-LFS, and the enhanced strip allows for the ultrasensitive quantitative assay of trace concentration of targets.

### 3.3. PEI-CISG-enhanced strip for p24 antigen detection

The proposed PEI-CISG-enhanced strip was first used for the ultrasensitive detection of p24 antigen (Fig. 3a), which is the earliest emerging protein biomarker in HIV-infected patients (Chai et al., 2017). The improved detection for p24 antigen can shorten the window period of acute HIV infection to enable early intervention and decrease virus transmission. Several key parameters affecting the detection sensitivity of AuNP-LFS, including the labeling pH value and amounts of anti-p24 detection Abs (dAbs) on the AuNPs, concentrations of AuNP@dAb

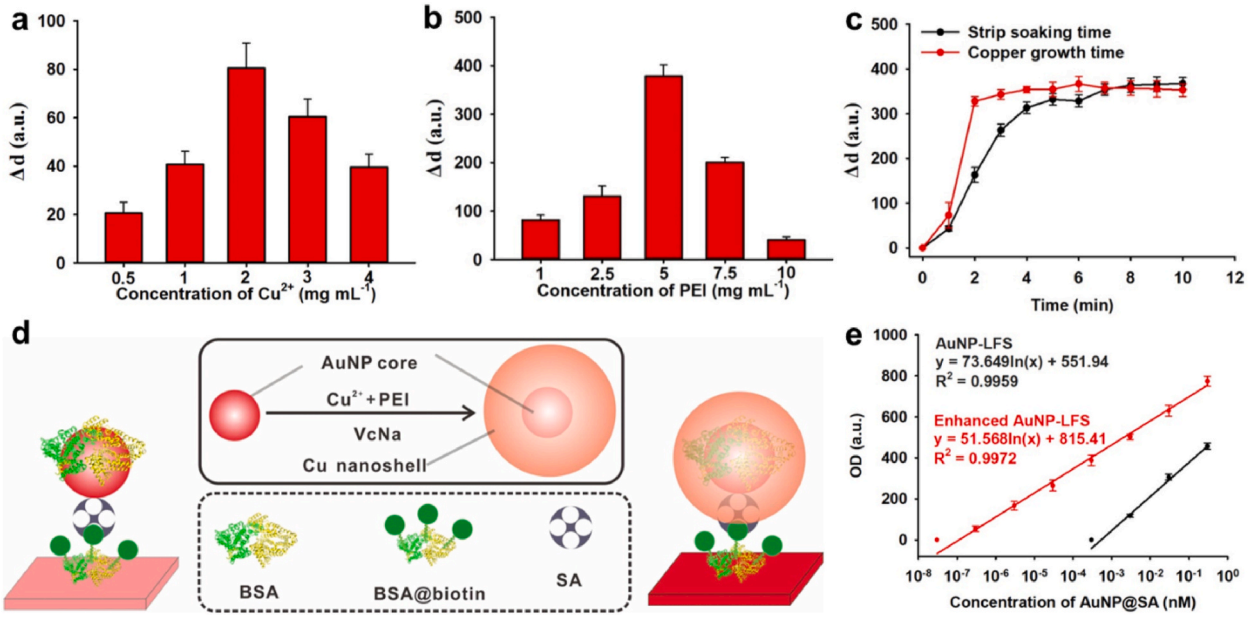


**Fig. 2.** Optimization of work conditions for PEI-CISG technology. Optimization for the concentrations and ratio of PEI and $Cu^{2+}$: (a) $Cu^{2+}$concentration at a given PEI concentration of 1 mg $mL^{-1}$, and (b) PEI concentrations under the optimal ratio of $Cu^{2+}$ and PEI. (c) Optimization for strip soaking time in PEI@$Cu^{2+}$ complex and copper growth time. (d) Schematic representation of PEI-CISG technology for enhanced AuNP-LFS *via* biotin-SA system. (e) Evaluation for signal amplification potential of our proposed PEI-CISG on AuNP-LFS platform *via* biotin-SA system.

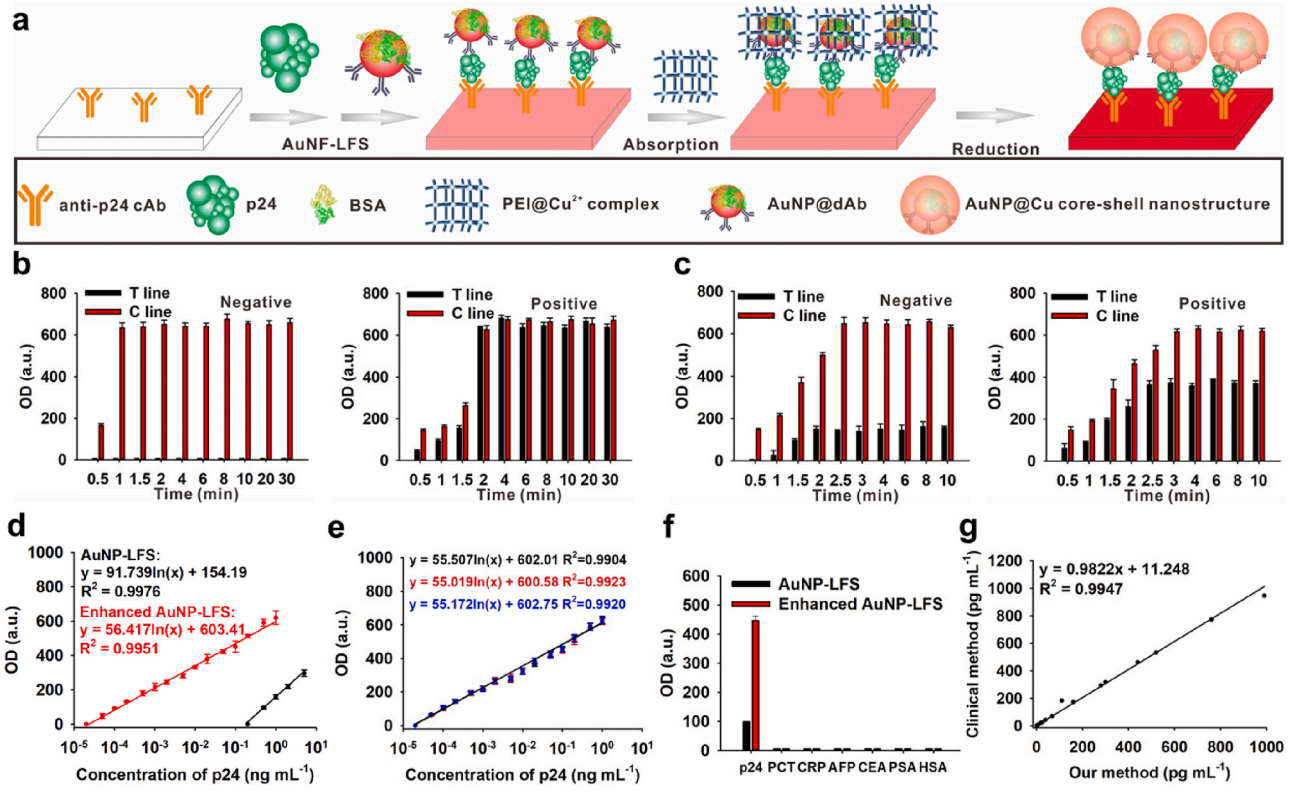


**Fig. 3.** A PEI-CISG enhanced AuNP-LFS for the detection of p24. (a) Schematic of PEI-CISG enhanced AuNP-LFS workflow for testing p24. A direct comparison of the proposed PEI-CISG on AuNF-LFS with conventional CISG: (b) PEI-CISG and (c) conventional CISG. The positive detection was conducted by using the sample solution containing 3.0 ng $mL^{-1}$ to run the strip, while the negative test was performed using blank control solution without p24. (d) The calibration curves of AuNP-LFS and PEI-CISG enhanced AuNP-LFS for detection of p24. These curves were plotted by recording specific response against p24 concentration. (e) Reproducibility analysis of PEI-CISG enhanced AuNP-LFS for the detection of p24. Three standard curves were established by measuring a series of different concentrations of p24 in the succeeding 3 days. (f) Specificity evaluation of the PEI-CISG enhanced AuNP-LFS for p24 detection by collecting the signal response against p24 at 0.5 ng $mL^{-1}$, and other protein markers of HSA, PSA, CEA, AFP, CRP, PCT at 500 ng $mL^{-1}$. (g) A correlation comparison of the PEI-CISG enhanced AuNP-LFS with the clinically used p24 chemiluminescence assay kits in simultaneously analysing 17 p24-positive human serums with the concentrations ranging from 1.8 to 990 pg $mL^{-1}$.

probe for p24, and anti-p24 captured Abs (cAbs) on the T line, were systematically investigated and optimized (Fig. S7 and Table S2). The optimized parameters for the preparation of AuNP-LFS were as follows: the pH of dAb-labeled AuNPs was 6.0; the labeled amount of dAbs on per milliliter AuNP solution was 2.0 μg; the concentrations of anti-p24 cAbs on the T line and AuNP@dAb on the conjugate pad were 1 mg $mL^{-1}$ and 30 pM, respectively. Under optimum conditions, we first evaluated the reliability of the PEI-CISG-enhanced strip by analyzing the dynamic process of colorimetric signal amplification on the NC membrane and T line at p24 antigen concentration of 0 and 3.0 ng $mL^{-1}$, respectively. The conventional CISG method without PEI regulation was used for comparison. Fig. 3b-c and Fig. S8 show that both of the enhanced strips for p24 positive sample (3.0 ng $mL^{-1}$) and their ODs on the T and C lines can quickly reach the maximum values within a short copper growth time of 2 and 4 min for the PEI-CISG and CISG method, respectively. However, the enhanced strip evidently presented a red band on the T line for the p24 negative sample after 1 min treatment with the CISG method, whereas the PEI-CISG strategy showed no signals on the T line within 30 min. In addition, compared with the PEI-CISG strategy, the CISG method showed stronger background color over the whole NC membrane. These results further confirm that PEI can suppress the self-nucleation of $Cu^{2+}$ when copper reduction is absent from the AuNPs as the promoter (Grzelczak et al., 2008). Conversely, $Cu^{2+}$ could promote self-nucleation without PEI regulation, thereby resulting in a false positive signal on the T line. Subsequently, the AuNP-LFS with or without PEI-CISG was used to detect a series of standard solutions with p24 concentrations ranging from 0 fg $mL^{-1}$ to 5 ng $mL^{-1}$. Fig. S9 and Fig. 3d reveal the prototypes of the reacted strip and the corresponding OD values at the T lines. The results in Fig. S9 exhibit that the visual LOD (vLOD) of the unamplified AuNP-LFS for p24 antigen detection was 2 ng $mL^{-1}$, which is defined as the lowest p24 concentration to generate a visual red band on the T line. After the strip was treated by the PEI-CISG strategy, the vLOD of the enhanced strip dropped to 50 fg $mL^{-1}$, which was over four orders of enhanced sensitivity than that of the AuNP-LFS before amplification. In addition, the LOD value is comparable to or even better than those obtained by other groups (Table S3). The result in Fig. 3d indicates an excellent linear dependence between the OD values and the logarithmic concentration of p24 with a wide concentration range of 50 fg $mL^{-1}$ to 1 ng $mL^{-1}$. Three identical standard curves were established in the succeeding 3 days to estimate the reproducibility of the PEI-CISG method. The results in Fig. 3e show the excellent consistency among the three independent amplified tests with coinciding calibration curves and similar slopes of 55.507, 55.019, and 55.172. Additionally, a p24 protein-spiked sample (625 fg $mL^{-1}$) was simultaneously measured and analyzed using these three calibration curves. The p24 concentrations in this sample were 614.71, 628.19, and 604.77 fg $mL^{-1}$ with a small variable coefficient of 1.90%, showing the excellent reproducibility of the PEI-CISG method for amplifying the optical signal of the strip at different times and in various batches. Fig. 3f and Fig. S10 show that the enhanced strip maintained the outstanding discrimination capacities for p24 antigen against six other serum protein biomarkers. The detection results obtained by using the PEI-CISG method agreed with those from a clinically used chemiluminescence method that simultaneously analyzed 17 serum samples (Fig. 3g). These findings demonstrate the huge potential of our PEI-CISG method to enhance the sensitivity of AuNP-LFS with acceptable reliability, reproducibility, and selectivity for

the early diagnosis of HIV infection in resource-limited regions.

### 3.4. PEI-CISG-enhanced strip for E. coli O157:H7 detection

*E. coli* O157:H7 has been considered one of the major public health threats, leading to serious infectious diseases mainly through contaminated water and food (Eppinger et al., 2011). Numerous countries and regions have set up the "zero tolerance" standard to control *E. coli* O157:H7 contamination (Fagerquist et al., 2010). Thus, a sensitive and rapid diagnosis of *E. coli* O157:H7 detection is imperative. Here, we further explored the application of our developed PEI-CISG-enhanced strip for sensitive *E. coli* O157:H7 determination in milk (Fig. 4a). The dAbs and cAbs against *E. coli* O157:H7 were used for the preparation of AuNP@dAb probes and sprayed on the NC membrane as the T line. The optimization of AuNP-LFS for *E coli* O157:H7 detection is described in Fig. S11 and Table S4. Under optimum conditions, the strips before and after PEI-CISG treatment were employed to detect *E. coli* O157:H7 in various standard solutions with concentrations from 0 CFU $mL^{-1}$ to 9.60 × $10^5$ CFU $mL^{-1}$. The *E. coli* O157:H7 standard solutions were prepared by adding *E. coli* O157:H7 stock solution into 10-fold diluted milk. The strip stereograms in Fig. S12 reveal that the vLOD of AuNP-LFS before PEI-CISG treatment was 3.84 × $10^3$ CFU $mL^{-1}$. After signal amplification, the vLOD of the enhanced strip remarkably decreased to 6.0 CFU $mL^{-1}$, whereas no bands were observed in the test of all three *E. coli* O157:H7 negative samples. This LOD value is better than most reported protocols in detecting *E. coli* O157:H7, as shown in Table S5. Additionally, one of the three enhanced strips showed no red band on the T line when the *E. coli* O157:H7 concentration was 6 CFU $mL^{-1}$. This phenomenon possibly occurred due to the absence of bacteria in 75 μL aqueous solution given the presence of large dilution errors, which coincided with the Poisson–Binomial distribution model. About 1 mL 10-fold diluted milk samples containing 90 and 9 CFU *E. coli* O157:H7 were divided into 13 equal aqueous solutions, and all of the samples were tested by using the PEI-CISG-enhanced strip to further verify this assumption. Fig. 4b shows that all 13 samples tested positive when *E. coli* O157:H7 concentration was 90 CFU $mL^{-1}$, whereas 4 out of 13 samples tested positive when *E. coli* O157:H7 concentration was 9 CFU $mL^{-1}$, demonstrating the great potential of the PEI-CISG-enhanced strip in detecting ultralow concentrations of *E. coli* O157:H7, including a single bacterial cell in 75 μL sample solution. The quantification calibration curves for *E. coli* O157:H7 were plotted by using the OD value of the strips before and after signal amplification against the logarithmic *E. coli* O157:H7 concentration (Fig. 4c). The selectivity of the enhanced strip was further evaluated by analyzing 18 common pathogenic bacterial strains. The results in Fig. 4d show that a specific positive response was only observed in the tested *E. coli* O157:H7-spiked milk sample (6 × $10^4$ CFU $mL^{-1}$) but not in other control bacteria (6 × $10^5$ CFU $mL^{-1}$), indicating the excellent selectivity of PEI-CISG-enhanced strip for *E. coli* O157:H7. Further addition and recovery tests showed the acceptable accuracy and precision of the PEI-CISG-enhanced strip for *E. coli* O157:H7 quantification in real milk samples (Table S6).

### 3.5. PEI-CISG-enhanced strip for improved SARS-CoV-2 infection diagnosis

The accuracy, applicability, reliability, and universality of our PEI-CISG method have been well characterized with p24 antigen and *E. coli* O157:H7. However, these studies were only completed under laboratory conditions. The mandatory evaluation for clinical diagnostic efficacy should be further conducted by clinical studies. In addition, the compatibility characterization of our PEI-CISG method with the commercial AuNP-LFS strip extends the application scope and value of our

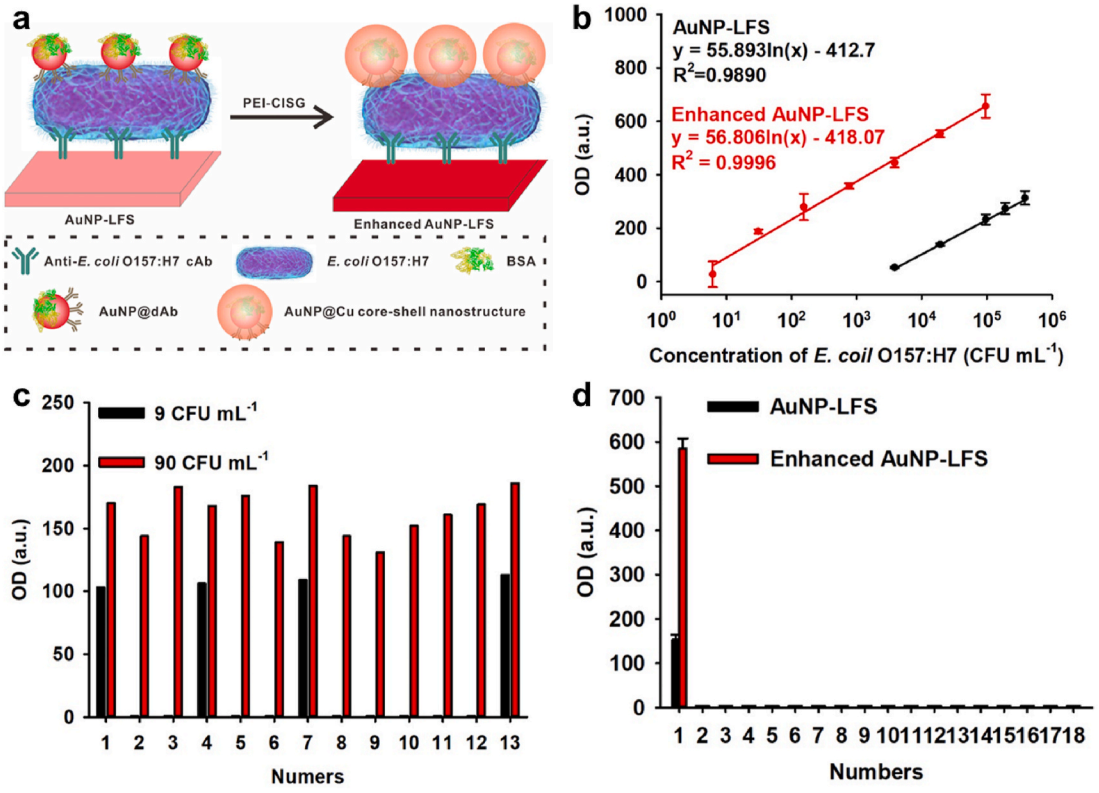


**Fig. 4.** Application of PEI-CISG enhanced AuNP-LFS for the detection of *E. coli* O157:H7. (a) Schematic illustration of PEI-CISG enhanced AuNP-LFS for detecting *E. coli* O157:H7. (b) The standard curves for conventional AuNP-LFS and the amplified PEI-CISG strip. The curve was constructed by analyzing a series of different concentrations of *E. coli* O157:H7 ranging from $10^0$ CFU $mL^{-1}$ to $10^6$ CFU $mL^{-1}$. (c) Reliability evaluation of the PEI-CISG enhanced AuNP-LFS for the detection of *E. coli* O157:H7 at ultralow concentrations of 9.0 × $10^1$ CFU $mL^{-1}$ and 9.0 × $10^0$ CFU $mL^{-1}$. (d) Specificity analysis for our enhanced AuNP-LFS strip by recording the responses against *E. coli* O157:H7 and other non-target bacteria.

method. COVID-19 has spread quickly all over the world and developed into an outbreak (Rao et al., 2020), posing a global public health concern since it was first reported. SARS-CoV-2 has been identified as the infecting pathogen. Thus, a sensitive, rapid, and accurate detection method for SARS-CoV-2 infection diagnosis is urgently needed to control virus transmission and assure timely treatment of patients. Given this need, we further conducted clinical studies by integrating our PEI-CISG strategy with a commercial AuNP-LFS detection kit for SARS-CoV-2 Abs based on the double-antigen sandwich format. A positive blood sample collected from COVID-19 patients confirmed by using RT-PCR was first employed to evaluate the amplification efficiency of our PEI-CISG method on commercial strips. The blood sample was continuously diluted by factors of 1:10, 1:20, 1:40, 1:80, 1:200, 1:400, 1:1000, 1:2000, 1:4000, 1:8000, and 1:16000 using the sample-loading solution packaged in the strip kit. The original blood sample and all diluted samples were simultaneously measured by using the commercial strip with or without the PEI-CISG treatment. A negative control test was conducted by using the sample-loading solution. Fig. 5a indicates that a visible red band on the T line was observed when testing these samples with a dilution factor of less than 1:20 by using the commercial strip without the PEI-CISG treatment. By contrast, a visible red band on the T line was observed in the diluted samples with a factor of 1:2000 after the PEI-CISG amplification was integrated, indicating the feasibility of our proposed PEI-CISG in enhancing the commercial AuNP-LFS. No bands appeared at the T area when measuring the negative control before or after treatment. These findings suggest that the PEI-CISG technique can effectively enhance the responsiveness of the commercial strip to samples with low target concentration, thus increasing the testing accuracy and decreasing the false negative rates. The clinical detection sensitivity and specificity of this method were further estimated using the blood samples collected from 69 clinically PCR-confirmed SARS-CoV-2-infected positive and 63 non-SARS-CoV-2-infected negative patients at the First Affiliated Hospital of Nanchang University. Fig. 5b summarizes the test results of the commercial strip without PEI-CISG treatment. Among the 69 blood samples from SARS-CoV-2-infected patients, 62 and 7 samples tested positive and negative, respectively, by using this commercial strip method, leading to a sensitivity of 89.9%. All 63 blood samples from the negative patients tested negative, indicating a specificity of 100%. These results show the high consistency of this commercial method with the PCR approach in detecting COVID-19. Nonetheless, 7 false negative results (i.e., S3, S4, S5, S6, S7, S8, and S9, Fig. 5b) were obtained, and they were not successfully tested by directly using the commercial kit. However, all 7 pseudo-negative samples were successfully tested positive after PEI-CISG amplification (Fig. 5c). Notably, three randomly selected negative samples (S1, S2, and S10) used as the negative control still tested negative after the same PEI-CISG amplification, showing the feasibility of our amplified technology to eliminate false negatives but without false positives. These observations prove that our PEI-CISG signal amplification technology is conducive to enhancing the detection performance of the commercial AuNP-LFS for improved SARS-CoV-2 diagnosis. Further work should focus on expanding the test range and the sample number to validate the clinical efficacy of our PEI-CISG-enhanced strip.

## 4. Conclusions

In conclusion, we reported a controlled PEI-CISG signal amplification strategy and demonstrated its potential in improving the detection sensitivity of conventional AuNP-LFS. In this design, the controlled PEI-CISG was achieved by introducing PEI as SDA. By virtue of the metal coordination reaction between PEI and $Cu^{2+}$, $Cu^{2+}$ can be adsorbed onto the surface of AuNP probe by soaking the strip in a solution of PEI@$Cu^{2+}$ complex, in which PEI was employed to regulate the thermodynamics of anisotropic Cu nanoshell growth on the AuNP surface, thereby controlling the shape and size of the resultant AuNP@Cu core–shell nanostructures. PEI acted as stabilizer to confine free reduction and self-nucleation of $Cu^{2+}$, thereby eliminating background signal and reducing the risk of false positives. The PEI-CISG-enhanced AuNP-LFS strip achieved an ultrasensitive detection for p24 and *E. coli* O157:H7 with the LOD values of 50 fg $mL^{-1}$ and 6 CFU $mL^{-1}$, respectively. The

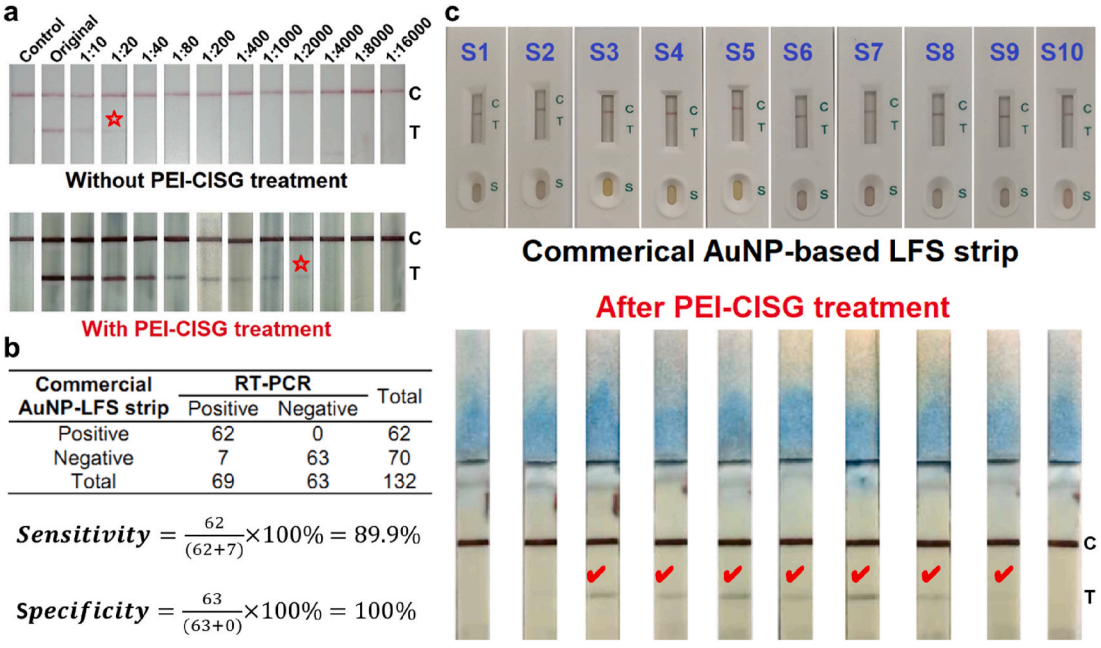


**Fig. 5.** The integration of commercial AuNP-LFS strip with our proposed PEI-CISG technology for the detection of SARS-CoV-2 Abs. (a) Evaluation of the detection ability of commercial AuNP-LFS strip with or without PEI-CISG treatment. A SARS-CoV-2-positive serum sample was continuously diluted by different factors, and then all diluted samples were simultaneously analyzed by using commercial AuNP-LFS strip with or without PEI-CISG treatment. (b) Performance characteristics of commercial AuNP-LFS strip. 132 clinical samples, including 69 positives and 63 negatives were tested using commercial AuNP-LFS strip. 7 PCR-confirmed SARS-CoV-2 positive samples were not successfully tested by commercial AuNP-LFS strip. (c) Improved evaluation of the commercial AuNP-LFS strip combined with PEI-CISG treatment for differentiating false negatives. "√" indicates the positive detection.

enhancement factor of our proposed approach is comparable to or even better than other signal amplification strategies involved in LFS (Table S7). With the improved method, we conducted clinical studies to confirm the clinical diagnostic efficacy of the proposed method, and the results showed that the smart integration of our PEI-CISG technology with a commercial AuNP-LFS detection kit can effectively surmount the false negatives for improved SARS-CoV-2 diagnosis. Collectively, the PEI-CICG technology provides a versatile and portable signal amplification tool to improve conventional AuNP-LFS detection, and demonstrate great potential for sensitive, accurate, and field-deployable diagnostics of various infectious diseases.

Nonetheless, this work does have limitations. The two-step growth for PEI-CISG processing may result in high system error and increase the risk of test failure. Although the performance of our PEI-CISG technology in actual samples is well demonstrated, the number of samples for methodological evaluation is relatively limited. The challenge from the sample matrix, such as fresh *vs.* frozen blood and serum/plasma *vs.* whole blood poses a risk that is difficult to predict and mitigate. Further work should focus on the design of automated and miniaturized devices, such as microfluidic platform, to integrate the PEI-CISG technology for reducing potential human error, and improving assay efficiency, thus addressing the field performance risks.

## CRediT authorship contribution statement

**Yaofeng Zhou:** Writing - original draft, Data curation, is responsible for the main data curation and writing original draft. **Yuan Chen:** Data curation, is responsible for the part of data curation. **Yang Liu:** is responsible for the validation the clinical diagnostic efficacy of the proposed method for SARS-CoV-2 Abs. **Hao Fang:** Data curation, is responsible for the part of data curation. **Xiaolin Huang:** Conceptualization, Methodology, Writing - review & editing, paper, is responsible for the conceptualization, methodology, and reviewing & editing paper. **Yuankui Leng:** Data curation, is responsible for the part of data curation. **Zhengqiong Liu:** Methodology, is responsible for the validation the clinical diagnostic efficacy of the proposed method for SARS-CoV-2 Abs. **Li Hou:** Project administration, is responsible for the Project administration. **Wei Zhang:** Methodology, Funding acquisition, is responsible for the validation the clinical diagnostic efficacy of the proposed method for SARS-CoV-2 Abs and also provided the funding acquisition. **Weihua Lai:** Project administration, is responsible for the the Project administration. **Yonghua Xiong:** Writing - review & editing, Funding acquisition, proposed experimental design, instructed the students to complete their experiments, and revised the full paper. In addition, Dr. Xiong also provided the funding acquisition.

## Declaration of competing interest

The authors declare that they have no known competing financial interests or personal relationships that could have appeared to influence the work reported in this paper.

## Acknowledgements

The authors thank the funding of National Key Research and Development Program of China (2018YFC1602203 and 2018YFC1602202), National Natural Science Foundation of China (32001788, 31760485, 31901780), Interdisciplinary Innovation Fund of Natural Science, Nanchang University (9166-27060003-ZD01), Jiangxi Provincial Natural Science Foundation (20202ACB215004), and Opening Fund of Jiangsu Key Laboratory for Food Quality and Safety-State Key Laboratory Cultivation Base, Ministry of Science and Technology (028074911709). All human blood samples were obtained by the First Affiliated Hospital of Nanchang University (Nanchang, China), and the related experiments were approved by the Medical Ethics Committee of the First Affiliated Hospital of Nanchang University and the informed consent was signed by all involved patients.

## Appendix A. Supplementary data

Supplementary data to this article can be found online at https://doi.org/10.1016/j.bios.2020.112753.

## References

Aissa, A.B., Herrera-Chacon, A., Pupin, R., Sotomayor, M., Pividori, M., 2017. Biosens. Bioelectron. 88, 101–108.
Brangel, P., Sobarzo, A., Parolo, C., Miller, B.S., Howes, P.D., Gelkop, S., Lutwama, J.J., Dye, J.M., McKendry, R.A., Lobel, L., 2018. ACS Nano 12 (1), 63–73.
Cao-Lormeau, V.-M., Blake, A., Mons, S., Lastère, S., Roche, C., Vanhomwegen, J., Dub, T., Baudouin, L., Teissier, A., Larre, P., 2016. Lancet 387 (10027), 1531–1539.
Chai, Q., Jovasevic, V., Malikov, V., Sabo, Y., Morham, S., Walsh, D., Naghavi, M.H., 2017. Nat. Commun. 8 (1), 1–13.
Chen, R., Huang, X., Xu, H., Xiong, Y., Li, Y., 2015. ACS Appl. Mater. Interfaces 7 (51), 28632–28639.
Chen, X., Leng, Y., Hao, L., Duan, H., Yuan, J., Zhang, W., Huang, X., Xiong, Y., 2020. Theranostics 10 (8), 3737.
Chen, Z., Chang, J.W., Balasanthiran, C., Milner, S.T., Rioux, R.M., 2019. J. Am. Chem. Soc. 141 (10), 4328–4337.
Da Silva, R.R., Yang, M., Choi, S.-I., Chi, M., Luo, M., Zhang, C., Li, Z.-Y., Camargo, P.H., Ribeiro, S.J.L., Xia, Y., 2016. ACS Nano 10 (8), 7892–7900.
Duan, H., Huang, X., Shao, Y., Zheng, L., Guo, L., Xiong, Y., 2017. Anal. Chem. 89 (13), 7062–7068.
Eppinger, M., Mammel, M.K., Leclerc, J.E., Ravel, J., Cebula, T.A., 2011. Proc. Natl. Acad. Sci. U.S.A. 108 (50), 20142–20147.
Fagerquist, C.K., Garbus, B.R., Miller, W.G., Williams, K.E., Yee, E., Bates, A.H., Boyle, S. o.n., Harden, L.A., Cooley, M.B., Mandrell, R.E., 2010. Anal. Chem. 82 (7), 2717–2725.
Gao, Z., Ye, H., Tang, D., Tao, J., Habibi, S., Minerick, A., Tang, D., Xia, X., 2017. Nano Lett. 17 (9), 5572–5579.
Gonçalves, B.P., Kapulu, M.C., Sawa, P., Guelbéogo, W.M., Tiono, A.B., Grignard, L., Stone, W., Hellewell, J., Lanke, K., Bastiaens, G.J., 2017. Nat. Commun. 8 (1), 1–11.
Grout, A., Howard, N., Coker, R., Speakman, E.M., 2017. Lancet Infect. Dis. 17 (4), e118–e122.
Grzelczak, M., Pérez-Juste, J., Mulvaney, P., Liz-Marzán, L.M., 2008. Chem. Soc. Rev. 37 (9), 1783–1791.
Hao, L., Leng, Y., Zeng, L., Chen, X., Chen, J., Duan, H., Huang, X., Xiong, Y., Chen, X., 2020. Adv. Sci. 7 (2), 2070011.
Huang, D., Lin, B., Song, Y., Guan, Z., Cheng, J., Zhu, Z., Yang, C., 2018a. ACS Appl. Mater. Interfaces 11 (2), 1800–1806.
Huang, X., Aguilar, Z.P., Xu, H., Lai, W., Xiong, Y., 2016. Biosens. Bioelectron. 75, 166–180.
Huang, X., He, Z., Guo, D., Liu, Y., Song, J., Yung, B.C., Lin, L., Yu, G., Zhu, J.-J., Xiong, Y., 2018b. Theranostics 8 (13), 3461.
Huang, X., Zhou, Y., Ding, L., Yu, G., Leng, Y., Lai, W., Xiong, Y., Chen, X., 2019. Small 15 (51), 1903861.
Jiang, B., Duan, D., Gao, L., Zhou, M., Fan, K., Tang, Y., Xi, J., Bi, Y., Tong, Z., Gao, G.F., 2018. Nat. Protoc. 13 (7), 1506–1520.
Khalil, I.A., Troeger, C., Rao, P.C., Blacker, B.F., Brown, A., Brewer, T.G., Colombara, D. V., De Hostos, E.L., Engmann, C., Guerrant, R.L., 2018. Lancet Glob. Health 6 (7), e758–e768.
Khan, M.S., Osei-Kofi, A., Omar, A., Kirkbride, H., Kessel, A., Abbara, A., Heymann, D., Zumla, A., Dar, O., 2016. Lancet Infect. Dis. 16 (8), e173–e177.
Kim, J., Mohamed, M.A.A., Zagorovsky, K., Chan, W.C., 2017a. Biomaterials 146, 97–114.
Kim, J.H., Park, J.E., Lin, M., Kim, S., Kim, G.H., Park, S., Ko, G., Nam, J.M., 2017b. Adv. Mater. 29 (37), 1702945.
Kurdekar, A.D., Chunduri, L.A., Manohar, C.S., Haleyurgirisetty, M.K., Hewlett, I.K., Venkataramaniah, K., 2018. Sci. Adv. 4 (11), eaar6280.
López-Ríos, F., Illei, P.B., Rusch, V., Ladanyi, M., 2004. Lancet 364 (9440), 1157–1166.
Li, J., Zheng, L., Cai, H., Sun, W., Shen, M., Zhang, G., Shi, X., 2013. Biomaterials 34 (33), 8382–8392.
Liu, D., Huang, X., Wang, Z., Jin, A., Sun, X., Zhu, L., Wang, F., Ma, Y., Niu, G., Hight Walker, A.R., 2013. ACS Nano 7 (6), 5568–5576.
Loynachan, C.N., Thomas, M.R., Gray, E.R., Richards, D.A., Kim, J., Miller, B.S., Brookes, J.C., Agarwal, S., Chudasama, V., McKendry, R.A., 2018. ACS Nano 12 (1), 279–288.
Lu, Z., Liu, G., Phillips, H., Hill, J.M., Chang, J., Kydd, R.A., 2001. Nano Lett. 1 (12), 683–687.
Rao, L., Tian, R., Chen, X., 2020. ACS Nano 14 (3), 2569–2574.
Reiner, R.C., Welgan, C.A., Casey, D.C., Troeger, C.E., Baumann, M.M., Nguyen, Q.P., Swartz, S.J., Blacker, B.F., Deshpande, A., Mosser, J.F., 2019. Nat. Microbiol. 4 (12), 2310–2318.
Santiago, G.A., Vázquez, J., Courtney, S., Matías, K.Y., Andersen, L.E., Colón, C., Butler, A.E., Roulo, R., Bowzard, J., Villanueva, J.M., 2018. Nat. Commun. 9 (1), 1–10.
Skrabalak, S.E., Au, L., Li, X., Xia, Y., 2007. Nat. Protoc. 2 (9), 2182.
Sun, Y., Xia, Y., 2002a. Adv. Mater. 14 (11), 833–837.
Sun, Y., Xia, Y., 2002b. Science 298 (5601), 2176–2179.

Tang, D., Sauceda, J., Lin, Z., Ott, S., Basova, E., Goryacheva, I., Biselli, S., Lin, J., Niessner, R., Knopp, D., 2009. Biosens. Bioelectron. 25 (2), 514–518.
Tian, M., Lei, L., Xie, W., Yang, Q., Li, C.M., Liu, Y., 2019. Sensor. Actuator. B Chem. 282, 96–103.
Wang, H., Zhou, S., Gilroy, K.D., Cai, Z., Xia, Y., 2017. Nano Today 15, 121–144.
Washio, I., Xiong, Y., Yin, Y., Xia, Y., 2006. Adv. Mater. 18 (13), 1745–1749.
Wood, C.S., Thomas, M.R., Budd, J., Mashamba-Thompson, T.P., Herbst, K., Pillay, D., Peeling, R.W., Johnson, A.M., McKendry, R.A., Stevens, M.M., 2019. Nature 566 (7745), 467–474.
Xia, Y., Gilroy, K.D., Peng, H.C., Xia, X., 2017. Angew. Chem. Int. Ed. 56 (1), 60–95.
Xiao, Y., Wang, Y., Tang, Q., Wei, L., Zhang, X., Jia, G., 2018. Angew. Chem. Int. Ed. 57 (49), 15995–16000.
Xiong, Y., Washio, I., Chen, J., Cai, H., Li, Z.-Y., Xia, Y., 2006. Langmuir 22 (20), 8563–8570.
You, M., Lin, M., Gong, Y., Wang, S., Li, A., Ji, L., Zhao, H., Ling, K., Wen, T., Huang, Y., 2017. ACS Nano 11 (6), 6261–6270.
Zhan, L., Guo, S.-z., Song, F., Gong, Y., Xu, F., Boulware, D.R., McAlpine, M.C., Chan, W. C., Bischof, J.C., 2017. Nano Lett. 17 (12), 7207–7212.
Zhang, B., Pinsky, B.A., Ananta, J.S., Zhao, S., Arulkumar, S., Wan, H., Sahoo, M.K., Abeynayake, J., Waggoner, J.J., Hopes, C., 2017. Nat. Med. 23 (5), 548.
Zhou, Y., Ding, L., Wu, Y., Huang, X., Lai, W., Xiong, Y., 2019. Trends Anal. Chem. 112, 147–160.
Zhou, Y., Huang, X., Zhang, W., Ji, Y., Chen, R., Xiong, Y., 2018. Biosens. Bioelectron. 102, 9–16.